Influence of magma flux on magma storage depths along the Reykjanes Ridge

R.J.M. Baxter[1,2] and J. Maclennan[1]

[1]Department of Earth Sciences, University of Cambridge, Downing Street, Cambridge CB2 3EQ, UK

[2]Department of Geology, University of Otago, New Zealand

February 20, 2024

Abstract

Quantitative thermomechanical models of mid-ocean ridge magmatic systems focus on spreading rate variations as the principal control on crustal thermal structure and the distribution of melt storage. The Reykjanes Ridge (RR), a slow-spreading portion of the Mid-Atlantic Ridge, has a near-constant spreading rate, but crustal thickness varies by a factor of two. Therefore, magma flux to the ridge varies independently of spreading rate. Here, we investigate the role of magma flux on storage depths along mid-ocean ridges (MORs) and constrain the roles of mantle melt generation rate and spreading rate on oceanic crustal magmatic systems.

Using pyOPAM, an open-source Python script written to carry out olivine–plagioclase–augite–melt (OPAM) thermobarometry, with an uncertainty of 1.2 kbar and 9.7°C , samples between 64°N and 52.5°N are compared. The distribution of median OPAM pressure and temperature estimates are compared with calculated magma flux rates across the area of interest.

The section of the RR immediately south of the subaerial Reykjanes Peninsula has a median OPAM pressure of 3.7 kbar, and estimated magma flux of 8.82×10^{-6} km^3 km^{-2} y^{-1}. The southern end of the RR has a median storage pressure of 4.8 kbar, and magma flux of 4.58×10^{-6} km^3 km^{-2} y^{-1}. In comparison, The Charlie-Gibbs Fracture Zone to the south has a median OPAM estimate of 6.3 kbar and calculated magma flux of 2.71×10^{-6}km^3 km^{-2} y^{-1}. Despite important local variation, median final magma storage depths and temperatures before eruption increase southwards along the RR. This finding indicates that magma storage depths at mid-ocean ridges are controlled predominantly by magma flux rather than spreading rate alone. Increasing magma flux drives the shallowing of cooler, final magma

storage depths, and decreasing magma flux increases magma storage depths and temperature.

1 Introduction

Many studies have endeavoured to understand magma storage distribution and the factors controlling these depths, especially along Earth's largest magmatic system, MORs, which extend over 56,000 km across the planet and produce more than two-thirds of the annual volcanic output (Soule, 2015). They provide an important mechanism and interface for heat and chemical exchange between the Earth's interior, crust, oceans, and atmosphere (Lowell et al., 2008). Processes that influence the morphology and chemical characteristics of MORs can also influence oceanic current circulation (Garcia Berdeal et al., 2006) and changes to ocean chemistry (Elderfield and Schultz, 1996), in turn affecting marine ecosystems (Boehlert, 1988) and the wider Earth–ocean–atmosphere system.

Mid-ocean ridge magmatic systems provide an excellent opportunity to test and refine thermomechanical models of magmatic systems, such as the influential crustal-scale models of Annen et al. (2006) and Jackson et al. (2018). A crucial advantage of modelling mid-ocean ridge magmatic systems is that the long-term input flux of mass and heat from the mantle is well constrained. This flux can be obtained from knowledge of spreading rate and crustal thickness. In this case, other assumptions in the physical models regarding the relative motion of melt and solid and the petrological thermodynamics of the system can be tested by comparison of model results with petrological and geophysical observations (Cannat et al., 2004). Heat supply and transfer abilities within a hydrothermal system are reliant on the release of latent heat during cooling and crystallisation of basaltic magma (Sleep, 1975; Maclennan, 2008; Hasenclever et al., 2014). This, in turn, is controlled by the distribution of these intrusions (Maclennan, 2008) and the crustal thermal structure. Petrological estimates of the depths of magma storage have the potential to provide quantitative constraints on the distribution of heat sources and sinks in magmatic systems.

There is a well-established relationship between the depth of melt lenses at MORs and spreading rates (Herzberg, 2004; Macdonald, 2001; Carbotte et al., 1998; Michael and Cornell, 1998; Phipps Morgan and Chen, 1993; Morgan and Chen, 1993). Distinctive physical characteristics of spreading centres distinguish slow- and fast-spreading centres (Chen, 2003). Fast-spreading ridges with stable, long-lived magma supply are indicated by axial highs with smooth flank topography underlain by lens-like magma chambers at shallow depths, and coincide with increased crustal thickness and positive Bouguer gravity anomalies (Chen, 2003). Crustal thickness is relatively invariant on short length scales, and a warm thermal structure enables melt lenses to form and persist at upper crustal levels (Christeson et al., 2019; Carbotte et al., 2016, 1998; Phipps Morgan and Chen, 1993; Morgan and Chen, 1993; Lin and Phipps Morgan, 1992). Slow-spreading ridges are identified by axial rift valleys, with rough flank topography not typically underlain by long-lived melt lenses, highly variable crustal thickness, and negative Bouguer gravity anomalies. At intermediate- and slow-spreading ridges, magma supply is spatially and temporally variable, and heat loss results in a cool thermal structure (Bown and White, 1994). The median depth of crystallisation increases as the spreading rate decreases, associated with a spread in the dispersion of reported storage depths at a given spreading rate (Wanless and Behn, 2017; Searle et al., 2010; Bach and Früh-Green, 2010; Herzberg, 2004; Carbotte et al., 1998; Michael and Cornell, 1998; Phipps Morgan and Chen, 1993; Morgan and Chen, 1993; Purdy et al., 1992). Yet, despite these established relationships between spreading rate and storage depth, there are exceptions. Some portions of MORs are slow-spreading, yet display features of faster-spreading centres (thicker crust, positive Bouguer anomalies, steady topography). The Reykjanes Ridge (RR), a section of the Mid-Atlantic Ridge immediately south of Iceland, is a prime example. Previous petrological barometry of the RR indicated unusually shallow storage for a slow-spreading ridge, which was attributed directly to increased mantle temperatures in the vicinity of the Iceland plume (Herzberg, 2004). Recent work on Iceland has highlighted the role of magma

flux in controlling storage depths across the rift zones of the island (Baxter et al., 2023). This magma flux control appears to hold across volcanic systems where estimated variations in mantle potential temperature are relatively limited (Maclennan et al., 2001; Ito et al., 2003).

The aim of this study is to quantitatively constrain the relationship between magma flux and final magma storage depths at MORs, using the OPAM barometer. Basaltic melts saturated in olivine–plagioclase–augite vary in composition as a function of pressure (O'Hara, 1968; Kushiro et al., 1972; Kushiro, 1974; Michael and Chase, 1987; Grove et al., 1992). The position of the olivine–plagioclase–augite–melt (OPAM) cotectic moves as function of pressure, allowing the composition of basaltic glass to be used to estimate equilibration pressures of basaltic liquids (Yang et al., 1996; Hartley et al., 2018; Voigt et al., 2017). The most recent iteration of this barometer (Baxter et al., 2023) allows glass composition to be processed, and non-olivine– plagioclase– augite-saturated compositions to be filtered out, resulting in robust estimates for final depth of storage of magmas. This application of OPAM to magma storage depths along an MOR will constrain magma distribution variation in MOR settings. In doing so, this work aims to comment on the controls of this magma flux and improve current magma flux calculations, opening up the possibility to investigate storage distribution relationships in other volcanic settings, and to inform on processes involved in the source–sink abilities and distribution along spreading ridges.

2 Geological setting: Reykjanes Ridge

The RR is part of the Mid-Atlantic Ridge immediately south of Iceland (Fig. 1). This section of the Mid-Atlantic Ridge is slow-spreading with a half-spreading rate of 10 mm y^{-1}

on average (Minster and Jordan, 1978; DeMets et al., 2010). The ridge is tectonically continuous without major fracture zones for ∼1100 km between Iceland and the Bight Fracture Zone (Murton et al., 2002)). The RR is orientated 35°N, oblique to the direction of plate separation at 092°N (Talwani et al., 1971; Searle et al., 1998). Axial volcanic ridges, akin to *en echelon* fissure volcanoes in Iceland (Höskuldsson et al., 2007), are nearly orthogonal to plate motion and oblique to the RR itself (Searle et al., 1998). Where the RR shoals before becoming subaerial as the Reykjanes Peninsula in Southwest Iceland, the crust is 15 km thick (Weir et al., 2001), and reduces to 6.6 km at the southern end of the RR (Jones et al., 2014). Beyond the RR, crustal thickness decreases to 3.8 km thick at the Charlie-Gibbs Fracture Zone (Whitmarsh and Calvert, 1986).

The proximity to the Icelandic mantle plume results in physical and geochemical variations along the RR. Segmentation by transform faults is suppressed along the RR while morphological fluctuations include a shallow rise (between 60°N and 61°N), bathymetric undulations with 100 km wavelength, and nested, parallel V-shaped ridges (VSRs) and V-shaped troughs (VSTs) (Murton et al., 2002; Jones et al., 2002; Parnell-Turner et al., 2013; Jones et al., 2014). Over the length of the RR, crustal thickness fluctuates where VSRs and VSTs intersect the spreading axis (Jones et al., 2014). At 60.3°N, the intersection of the youngest VSRs and the spreading axis, wide-angle seismic experiments indicate that the crust is 10.0 ± 0.5 km thick (Smallwood and White, 1998). The corresponding trough at 58.5°N is estimated to be 7.8 ± 0.5 km thick. Free-air gravity anomalies present in the Mid-Atlantic Ridge indicate crustal thickness variation as VSRs and VSTs intersect the spreading axis (Sandwell and Smith, 2009; Parnell-Turner et al., 2013).

The VSRs and VSTs have been of particular interest to the MOR community (Vogt, 1971; Murton et al., 2002; Jones et al., 2002, 2014; Parnell-Turner et al., 2017); the VSRs

and VSTs to each side of the spreading ridge were first described by Vogt (1971). These V-shaped features have formed over the past 55 million years, recording fluctuations and pulses from the Icelandic plume (Parnell-Turner et al., 2014). The higher VSRs represent thicker portions of crust compared to associated VSTs (Jones et al., 2002; Parnell-Turner et al., 2013). The systematic variations of major, trace, and rare-earth elements for VSR rocks, observed up to 1350 km from Iceland (Jones et al., 2014), are generated primarily by changes in mantle potential temperature (White and McKenzie, 1995; Jones et al., 2002; Parnell-Turner et al., 2013). Migrating, hot pulses of outflowing mantle radiate away from the plume system, then, while propagating below the spreading ridge, are drawn up into the melting region, enhancing decompressional melting (Jones et al., 2002; Parnell-Turner et al., 2013; Jones et al., 2014). The increased melt supply leaves a V-shaped trail of thicker crust (Murton et al., 2002). The more northerly VSR intersecting the RR between 60°N and 61°N, where there is a slight rise in ridge elevation, coincides with an increasing number of seamounts, increasing size of axial volcanic ridges, a thicker crust, and positive free-air gravity anomaly (Searle et al., 1998; Smallwood and White, 1998; Parnell-Turner et al., 2017).

Major element trends and olivine–plagioclase–augite phenocryst assemblages indicate that the evolution of MOR-basaltic lavas along the RR are controlled by the fractionation of olivine, plagioclase, and augite (Murton et al., 2002), ideal for applying OPAM barometry (Grove et al., 1992; Yang et al., 1996). Compositional variations in VSRs cannot be explained by fractional crystallisation alone (Jones et al., 2014). The nearby Icelandic plume has a pronounced geochemical influence on incompatible element concentrations and isotope signatures in rocks produced by the RR (Jones et al., 2014; Murton et al., 2002; Schilling, 1973). Some isotopic signatures that have been linked to a plume persist up to 1000 km south of Iceland (Poreda et al., 1986; Hilton et al., 2000).

3 Methods

For this study, pyOPAM (Baxter et al., 2023) was applied to a dataset of glass and whole-rock major element composition, compiled from the literature and the PetDB Database (www.earthchem.org/petdb, October 2021). The following parameters were used to search the PetDB database: rock classification = basalt, between latitudes 51.80 to 64.00°N and longitude -35.40 to -21.60°W. This area was selected to contrast magma storage depths along an uninterrupted spreading axis (a signal of higher magma supply) and a spreading axis segmented by fracture zones (indication of low magma supply). From the PetDB samples and a further 282 samples from the Reykjanes Peninsula (acquired from the Iceland dataset compiled for Baxter et al. (2023)), 1582 were initially compiled for this study (Fig. 1). The contrasting conditions between these sites highlight the variable influence of additional melt supply along the MOR due to the effects of the Icelandic plume, and where this influence dissipates and fracture zones resume.

This compilation includes whole-rock and glass analyses. Melt inclusions are excluded because they sample liquids from an entire plumbing system, while the goal of this study is to investigate the shallowest storage depths at MORs. Glass analyses are preferred when applying OPAM barometry. In some locations, however, few glass analyses are reported, but whole-rock compositions are available. Whole-rock compositions are included because pyOPAM filters can remove samples that are affected by crystal accumulation and deviation from cotectic liquids (Baxter et al., 2023). This was demonstrated in Baxter et al. (2023), where variable abundances and proportions of phenocrysts were added back into experimental glass compositions. This modelling found that adding an excess 3% of extra olivine, plagioclase, and/or clinopyroxene crystals into the glass resulted in the modelled composition being removed by internal pyOPAM filters.

This dataset was then run through the pyOPAM code. There are three different steps of filtering within this Python script to ensure that the resulting pressure estimates are robust. The first filter removes any samples with <4 wt% MgO, as these compositions were inappropriate for this basaltic liquid barometer. The second filter is a statistical filter, first used in the implementation of Hartley et al. (2018), then in Baxter et al. (2023), to ascertain if melt compositions were three-phase saturated. The first step of this implementation calculates the χ^2 misfit between measured X_{Mg}, X_{Ca}, and X_{Al} content and those predicted by Yang et al. (1996). The misfit χ^2 is calculated using the following standard expression:

$$\chi^2 = \sum_{i=1}^{3} \left(\frac{X_i - Y_i}{\sigma_i} \right)^2 \tag{1}$$

where X_i are the measured cation fractions of Mg, Ca, and Al, and Y_i are those predicted, while σ is the analytical uncertainty on glass measurements by EMPA, estimated as ±5% for major element oxide components (Neave et al., 2015). Equations 1–3 from Yang et al. (1996) were then used to estimate the Y_i as a function of pressure and other measured sample compositional properties (X_{Si}, X_{Fe}, X_{Ti}, X_{K}, X_{Na}) ,and functions 1–3 from Table 2.15, (Yang et al., 1996), were used to return the pressure that minimised the χ^2 misfit. The quality of fit between the observed and predicted melt compositions is evaluated using the minimum χ^2. The resulting probability of fit (P_F) allows for the melt compositions to be assessed for three-phase saturation, and, thus, the calculated OPAM equilibration pressures to be assessed for robustness. Compositions with a $\mathrm{P}_F \geq 0.80$ were retained, but those with P_F <0.80 were interpreted as not three-phase saturated and were removed from the dataset; for further discussion, see (Hartley et al., 2018; Baxter et al., 2023). A final composition filter is used in the pyOPAM code, using the minimum FeOt wt%, CaO wt%, and Al_2O_3 wt% of the experimental basalts used in the original Yang et al. (1996) parameterisation,

removing samples with <7.9 FeOt wt%, <8.6 CaO wt%, and <11.15 Al_2O_3 wt%, eliminating remaining outliers.//

After the dataset was passed through pyOPAM, any samples from off-axis localities were removed so that further analysis of the dataset would remain focused on investigating the relationship between magma storage depths and the melt supply below the MOR axis. The remaining samples were then organised by location. The Reykjanes Peninsula comparison includes samples from the Svartsengi–Reykjanes volcanic system, Krysuvik volcanic system, and Brennisteinfjoll volcanic system. RR samples are on-axis-only samples, including samples from the two VSRs and corresponding VSTs. The Transitional/Bight Fracture Zone and Charlie-Gibbs Fracture Zone groups includes on-axis samples from where the RR transitions into the Bight Fracture Zone, then the MOR segment southwards until the next fracture zone, the Charlie-Gibbs Fracture Zone.

3.1 Thermobarometer implementation

pyOPAM (Baxter et al., 2023) was previously presented using only the Yang et al. (1996) barometer, which is independent of temperature, instead relying on iteratively solving three simultaneous equations to find pressure. We now include their geothermometer. After statistical filtering is carried out to assess the reliability of the pressure estimate, the pressure is incorporated into the fourth equation from Yang et al. (1996):

$$\begin{aligned} T = 581.7 + 5.858P - 691.0X_{Na} - 848.9X_K + 11492X_{Ti} - 574.3X_{Fe} \\ +3114X_{Si} - 3529X_{Si}^2 - 25679(X_{Si} \times X_{Ti}) \end{aligned} \tag{2}$$

where T is the temperature ($^\circ C$) , P is the pressure (kbar), and X_{Na}, X_K, X_{Ti}, X_{Fe},

and X_{Si} are the cation mole fractions of Na, K, Ti, Fe, and Si, as described.

3.2 Test dataset

We validated this geothermometer in our pyOPAM code with a test dataset of 250 experimental glass compositions that were compiled from the literature (Appendix 1). Experiments took place over a range of conditions (P = 0.001–14 kbar, T = 1062–1265°C) for a range of compositions (1.01–9.5 wt% alkalis). Compositions and conditions cover a slightly wider range than was originally used for the Yang et al. (1996) calibration, which included conditions of 0.001–10 kbar, 1020–1275°C, and 0–8.43 wt% Na_2O, 0-5.45 wt% K_2O). Olivine, plagioclase, and clinopyroxene phases were observed (± one of spinel, magnetite, or ilmenite). The 92 samples that passed pyOPAM statistical filtering set to $P_F \geq 0.80$ (see Baxter et al. (2023) for discussion of this threshold) produced a mean absolute error (MAE) of 9.7°C for estimated temperature (Fig. 2).

3.3 Extracting block-medians

Samples were processed in PyGMT (Tian et al., 2023) to visually demonstrate spatial distributions and relationships between OPAM depth estimates and sample sites along the Reykjanes Peninsula, RR, Bight Fracture Zone, and Charlie-Gibbs Fracture Zone. The function pyGMT.track was used to extract elevation and bathymetric depths at sample origin (not the depths of the samples themselves if collected from core). Axial volcanic ridges along the RR spreading ridge are suggested to represent the off-shore equivalents of volcanic systems along the Reykjanes Peninsula (Höskuldsson et al., 2007). Axial volcanic ridge abundance and scale are linked to magma supply feeding the MOR (Pałgan et al., 2017). Axial volcanic

ridges have been reported to range from 5–38 km in length, are 1.9–15 km wide, are spaced 1.5–12.3 km apart, and can be obliquely aligned (Pałgan et al., 2017; Parson et al., 1993; Höskuldsson et al., 2007; Parnell-Turner et al., 2013; Le Saout et al., 2023). Axial volcanic ridge systems overlap neighbouring systems by up to one-third of their length (Pałgan et al., 2017).

Median OPAM estimates were collected for areas of 50 km × 15 km, using the pyGMT.blockmedian function in PyGMT. This set area size was selected to 1) inspect variation between axial volcanic ridges along the RR; and 2) to find the ideal range to smooth individual axial volcanic ridges (which can be up to 15 km wide and 38 km long) signals and to observe the larger scale relationships between spreading rate, magma storage depths, and magma flux. For the subaerial comparison on the Reykjanes Peninsula, a single, slightly larger, block was used, of 50 km × 45 km, due to the oblique rifting nature along the peninsula. This block only captured samples from the footprint of the Svartsengi–Reykjanes volcanic system.

For converting pressure estimates to depth, we assume that oceanic crust is, on average, 8 km thick across the study area with a density of 3000 kg/^{3} (Weller et al., 2019), while underlying mantle lithosphere has a density of 3300 kg/^{3} (Weller et al., 2019). For samples on the Reykjanes Peninsula, pressure to depth estimates were made, assuming two distinct layers in the Icelandic crust (Jenkins et al., 2018). The upper 20 km of crust is estimated to have an average density of 3000 kg/m^3, while the lower crust is estimated to have a density of 3050 km/m^3 Darbyshire et al. (2000).

The median OPAM pressure and depth estimates could then be compared with magma flux, calculated for the same set regions.

3.4 Magma flux valculations

The magma flux is coarsely quantified across the study area and compared with final storage depths. Calculation of volumetric magmatic flux was performed by Paterson et al. (2011), following the typical flux definition of a volume passing through a set area over a period of time (e.g., $km^3\ km^{-2}\ y^{-1}$). A similar, simple approach is taken to assess the relationship between magma flux and storage depths. Median OPAM estimates were collected for 50 km $\times$ 15 km blocks using the blockmedian function in PyGMT (Tian et al., 2023) across the entire study area (RR to Charlie-Gibbs Fracture Zone). This set area is used for these flux calculations. Full spreading rates range from 21.4 mm/y at the Charlie-Gibbs Fracture Zone and decrease northwards to 18.8 mm/y (Minster and Jordan, 1978; DeMets et al., 2010). Crustal thickness estimates, ranging from 15 km at the southern end of the Reykjanes Peninsula to 3.8 km thick at the Charlie-Gibbs Fracture Zone, were obtained from the seismic surveys and crustal thickness models of (Whitmarsh and Calvert, 1986; Weir et al., 2001; Jones et al., 2014). More details can be found in Appendix 2.

The magma flux per unit area, M_Q, is defined as

$$M_Q = \frac{uh}{W} \tag{3}$$

where u is the full spreading rate, h is the crustal thickness, and W is the across-axis width of the zone of magmatic accretion. This width was fixed to 15 km to allow for overlapping systems to be smoothed out. For direct comparison with the block-median estimates for OPAM storage depths, M_Q was averaged over corresponding along-axis block lengths.

4 Results

Although some studies report the presence of olivine–plagioclase–augite phases and their control on the liquid line of descent (Murton et al., 2002), this is not reported for all samples available on PetDB (e.g., Melson (2003), Smithsonian Volcanic Glass File). From the 1582 compositions compiled for pyOPAM analysis, 889 analyses returned a $P_F \leq 0.80$ and were, thus, removed from the dataset. Three-phase saturation is confirmed for all samples that pass the filter by comparing FeOt, CaO, and Al_2O_3 with MgO wt% to demonstrate that liquid lines of descent are mostly controlled by the removal of olivine, plagioclase, and clinopyroxene (Fig. 3). The CaO vs. MgO wt% plot shows outliers deviating away from the liquid line of descent, likely due to crystal accumulation, with anomalously high CaO wt% vs. MgO wt%, and low OPAM pressure estimates (-1.43 to 0.55 kbar). These were removed once identified, reducing the final number of filtered samples to 690.

4.1 Distribution of OPAM pressures and temperatures

The widest distribution of OPAM pressures coincides with higher topography and thicker crust, found on the Reykjanes Peninsula, and at VSRs on the RR (Fig. 4a). OPAM pressures on the Reykjanes Peninsula range from -2.4 kbar to 11.1 kbar, with the lower quartile, median, and upper quartile at 2.2 kbar, 3.9 kbar, and 6.6 kbar, respectively. The negative pressure estimates for about 10% of the Reykjanes Peninsula samples reflect a combination of low-pressure equilibration recorded in lava samples and the expected uncertainty on the barometer. As such, we retain these pressure estimates when extracting the statistical measures in order to avoid bias. The on-axis submarine portion of the MOR region of interest has a substantially smaller range of OPAM pressures, ranging from 0.5 kbar to 7.4 kbar, with the lower quartile, median, and upper quartile at 3.3 kbar, 4.1 kbar, and 4.7 kbar, respectively.

The increasing OPAM pressures coincide with decreasing elevation and decreasing crustal thickness (Fig. 4a; 5; 6). The range of pressure estimates increases again to 2.4–7.4 kbar between 53.5 °N and 52 °N, where the MOR is transected by fracture zones again. Magma storage temperature tends to increase with increasing storage pressure (Fig. 4b).

VSTs have a relatively narrow range of OPAM estimates (2.9 – 5.6 kbar), with lower quartile, median, and upper quartile values of 3.6 kbar, 4.1 kbar, and 5.1 kbar, respectively. In comparison, the VSRs have a wider range of pressure estimates (Fig. 4a), ranging from 3.1 kbar to 11.8 kbar, with lower quartile, median, and upper quartile of 4.3 kbar, 5.1 kbar, and 6.3 kbar, respectively. When the median pressure is taken for a 50 km long x 15 km wide segment, however, the median pressure for the VSRs is shallower than the median pressure for the corresponding VSTs (Fig. 4b).

4.2 Relationship between pressure and proximity to Iceland

There is a spatial relationship between increasing axial median OPAM pressure for magma storage, the range of pressures, and proximity to the mantle plume below Iceland (Fig. 4; 5a). Median OPAM pressures for axial samples increase southwards, with increasing distance from the mantle plume, and the range of pressures decrease (Fig. 4; 5a) along the RR. This coincides with thinning crust and decreasing ocean floor elevation (Fig. 6). While VSRs have increased range compared to other axial samples, the range of pressure estimates decreases for VSRs with increasing distance from Iceland (VSR-1 = 3.1 kbar to 11.9 kbar; VSR-2 = 3.6 kbar to 8.1 kbar). This overall decrease in range ceases southward to 57.5°N, until transform fractures resume as the Bight Fracture Zone, cross-cutting the MOR, and increase again southward after ∼54°N.

4.3 Inspecting magma flux and median OPAM pressures.

One median pressure representing the Reykjanes–Svartsengi volcanic system was used as the onshore representative to compare with median OPAM estimates along the spreading axis of the RR. Only on-axis samples are considered for investigating the relationship between magma flux and median OPAM depths, as off-axis (Fig. 1) samples may not reflect on-axis processes. Deepest median storage and lowest magma flux are estimated for samples from the Bight Fracture Zone and Charlie-Gibbs Fracture Zone (Fig.4; 5; 6). The median OPAM estimates for axial samples decrease northwards along the RR, with the shallowest median OPAM depth and highest magma flux calculated for the Reykjanes–Svartsengi volcanic system on the southwestern end of the Reykjanes Peninsula (Fig. 4c). The increasing magma flux and decreasing storage depths occur despite negligible changes to the spreading rate. For calculated magma fluxes, the obliquely rifting Reykjanes Peninsula has the highest magma flux calculated in this study and the widest range of OPAM pressures (-2.4 kbar to 11.1 kbar). Overall, median OPAM storage pressures and temperatures increase southwards along the RR southwards and are at their greatest for the Bight Fracture Zone and Charlie-Gibbs Fracture Zone (Fig. 4; 5; 6) while magma flux estimates decrease, reaching their lowest at the Bight Fracture Zone and Charlie-Gibbs Fracture Zone (Fig. 4; 5; 6). Aberrations of this trend occur for the VSRs and VSTs. Samples from the VSRs have a lower median storage pressure and temperature than other nearby on-axis samples, despite having the widest range in storage pressures (Fig. 4a; 4b). They also display a slight increase in magma flux (Fig. 4c), whereas VSTs have an increase in the range of median depths of storage, and higher temperatures, but a clear decrease in magma flux (Fig. 4c), especially VST-1. A paucity of samples precludes derivation of a reliable relationship for off-axis storage and magma flux.

5 Discussion

This study demonstrates, using OPAM thermobarometry, that median depths and temperatures of magma storage decrease with increasing magma flux, and vice versa, rather than in response to variations in spreading rate alone along the RR (Fig. 4; 6; 7).

The relationship between the depths of melt lens storage and spreading rate has been long recognised at MORs (Herzberg, 2004; Macdonald, 2001; Carbotte et al., 1998; Michael and Cornell, 1998; Phipps Morgan and Chen, 1993; Morgan and Chen, 1993). Early models indicate a nonlinear relationship between melt lens distribution and spreading rate, with melt lens distribution deepening with decreasing spreading rate (Phipps Morgan and Chen, 1993; Morgan and Chen, 1993). This relationship was interpreted to be the result of balance between heat supply from magma injection and heat loss by hydrothermal cooling. As slower spreading rates decrease melt input fluxes from the mantle, hydrothermal circulation is more effective (Phipps Morgan and Chen, 1993; Morgan and Chen, 1993; Chen and Morgan, 1996). Using the compiled dataset of Gale et al. (2013) and recalculating the final depths of storage for MOR segment using pyOPAM, the global relationship between MOR-basalt storage depths and spreading rate is demonstrated in Fig. 7. For the dataset of Gale et al., 2013, the range of storage pressure decreases with increasing spreading rate. Spreading ridges including Afar, Gakkel, the SW Indian Ridge, and other slow (<40 mm/y) rifting segments of the Mid-Atlantic Ridge also display a wide range of storage depths (Fig. 7). At intermediate- and slow-spreading ridges, magma production is spatially and temporally sporadic. Magma storage deepens and is more variable, with storage zones observed in the lower crust, the mantle, or not at all. (Wanless and Behn, 2017; Searle et al., 2010; Bach and Früh-Green, 2010; Herzberg, 2004; Carbotte et al., 1998; Michael and Cornell, 1998; Phipps Morgan and Chen, 1993; Morgan and Chen, 1993; Purdy et al., 1992). Samples from the RR (Fig. 7),

instead, demonstrate increasing storage depths with increasing spreading rate, counter to what has been suggested as standard behaviour for MOR melt lenses. We, instead, observe that decreasing storage pressure more clearly coincides with increasing magma flux (Fig. 4c; 7) due to the Icelandic plume.

This relationship between increased magma flux from the Icelandic plume and the response of magma storage depths is demonstrated again by VSRs and corresponding VSTs. The presence of VSRs intersecting the RR axis is expected to correspond to km-scale variations in crustal thickness and, therefore, magma flux. There is some indication that the median storage depths at the VSR intersections are slightly shallower than those in the adjacent parts of the spreading ridge, and this effect is clearer for the VSRs intersection centred at ∼60.5°N (Fig. 4b). These variations in storage depth, associated with magma flux variations related to VSRs, are consistent with the larger-scale relationship between magma flux and storage depths along the RR. Importantly, these variations in storage depth are linked to variations in magma flux that are demonstrably dominated by variations in crustal thickness, rather than spreading rate variability.

Figs. 5 and 6 demonstrate that along the axis of the RR, final temperature and depth of magma storage are correlated to magma flux variations, irrespective of the narrow spreading rate range (18.8–21.4 mm/y) along the ridge. It is this additional melt being generated that is increasing magma flux variations along the RR that demonstrate median storage depths responding to magma flux, controlled here by higher potential mantle temperatures rather than strictly spreading rate alone. Demonstration of these relationships invites further investigation of other sections of mid-ocean ridges with varying mantle potential temperatures. Across MORs worldwide, mantle potential temperatures are suggested to vary by 200°C as they intersect or pass near mantle hotspots (Dalton et al., 2014; Gale et al., 2014).

The fluctuation of magma storage depths is exhibited here to be controlled by magma flux rather than the rate of plate divergence alone (Wanless and Behn, 2017). A warm thermal crustal structure enables melt lenses to form in upper crustal levels, which is typically observed and recognised for fast-spreading MOR segments (Christeson et al., 2019; Carbotte et al., 2016, 1998; Phipps Morgan and Chen, 1993; Morgan and Chen, 1993; Lin and Phipps Morgan, 1992). If high magma flux is stable, a warm thermal structure can persist, resulting in the persistent lower magma storage pressures, such as for the East Pacific Rise (Carbotte et al., 1998), as well as a reduction in the range of these final depths of storage (Fig. 7). At slow-spreading ridges, controls on magma supply are more susceptible to other influences, as is such for the RR, where the higher mantle potential temperature from the Icelandic plume causes variation in the magma flux, especially apparent where VSRs and VSTs intersect the MOR. Samples south of the RR show an increase in storage median depth variability, although deepening overall (Fig. 4; 6). Spatially variable and temporally inconsistent melt supply would only occur in discrete locations along a slow-spreading axis, resulting in a cool thermal structure (Bown and White, 1994), making it more difficult for shallow melt lenses to persist. This higher sensitivity in this MOR segment to other factors driving magma flux has resulted in a wider range of median storage pressures and temperatures along the slow-spreading RR. Similar relationships may explain the wide distribution of pressure estimates of other slow-rifting segments of the Mid-Atlantic Ridge, Afar Rift, Gakkel Ridge, and SW Indian Ridge (Fig. 7). Magma storage depths and temperatures in these settings will vary accordingly to melt supply.

5.1 Broad implications

The resulting difference in magma storage arrangement and temperatures due to magma-flux variability may help inform volcano monitoring and hazard implications, therefore making this relationship valuable to understand. Seismicity generated by magma batches moving from deep storage upward through the crust allows for intrusions to be monitored more easily prior to eruptions (Soosalu et al., 2006, 2010). Cooler temperatures in shallow storage zones increase magma viscosity and this, in turn, influences magma ascent, degassing, and eruptive style (Lesher and Spera, 2015; Griffiths, 2000; Neal et al., 2019; Giordano and Dingwell, 2003; Cassidy et al., 2018). The relationship between magma flux and storage could be investigated for volcanoes within nondivergent tectonic settings, although additional parameters would need to be considered for improving the magma flux calculation. Some examples where the current approach to estimating magma flux does not work include the flank-zone volcanoes of Iceland, ocean island basalt volcanoes, and non-plume intraplate volcanoes. The East Volcanic flank zone in Iceland has negligible spreading yet contains two of the most productive volcanic systems in Iceland, Katla and Hekla (Thordarson and Larsen, 2007; Einarsson, 2008), and was also the origin of the 2010 eruption of Eyjafjallajökull, a recent example showing the potential impact of eruptions from this part of Iceland (Mazzocchi et al., 2010). For ocean island volcanoes capable of impacting nearby populations, such as Hawai'i, the Galápagos archipelago, and the Canary Islands, while the relationship between final depths of magma storage and magma flux has been identified (Gleeson et al., 2020), it has yet to be quantitatively constrained. This magma flux equation could also be expanded further to consider the role of hydrous phases for the volume of melt generated, in order to test the relationship between magma flux and storage depth distributions for arc volcanism and nonplume intraplate settings, where the role of hydrous phases in metasomatised lithosphere are suggested to be an important control of melt generation (Scott et al., 2014; Panter et al., 2018; Scott et al., 2020).

6 Conclusions

This study clarifies and quantitatively demonstrates that final depths of magma storage in MOR settings respond to magma flux variability, rather than simply to spreading rates. Contrary to what has been previously reported in the MOR literature, we find that magma storage depths do not decrease with increasing spreading rate along the RR and immediately adjacent spreading ridge segments. Instead, we demonstrate that the final depths of magma storage respond to magma flux variability. Increasing magma flux results in shallower depths for magma storage along the spreading ridge axis. Shallower magma storage depths also coincide with the cooler temperatures that these melts are stored at. This highlights the importance of understanding magma flux and the effects imparted on resulting magma storage depths and conditions, which, in turn, can play a role in any resulting eruption.

The relationship between magma storage depths and magma flux has been suggested in other volcanic settings, which has profound implications for ongoing volcano-monitoring efforts. This study quantitatively demonstrates that in MOR settings, magma flux controls magma storage depths and temperatures.

7 Acknowledgements

This work was supported by the Cambridge-Rutherford Memorial scholarship awarded by the Rutherford Foundation of the New Zealand Royal Society and Cambridge-Trust, and the Rutherford Scholarship awarded by Trinity College, Cambridge, to R.J.M. Baxter. We

thank Marie Edmonds, Eniko Bali, and Mike Palin for productive discussions, as well as David Peate and Michael Stock and Editor Chiara Petrone for their constructive reviews and feedback, which greatly improved the clarity of the manuscript.

8 Competing interests

The authors declare that they have no competing interests.

9 Data availability

Datasets of compiled analyses from LEPR (OPAM_Thermobarometry_test(RR).csv), PetDB, and the wider literature(ReykRidge.csv), as well as the Jupyter Notebooks for the test dataset (pyOPAM Thermobarometry_test(RR).ipynb) and to execute the analysis in the paper (Reykjanes_Ridge_pyOPAM.ipynb), can be found and are hosted at: *https://github.com/Rjmbx/pyOPAM*.

Figures

References

C. Annen, J. D. Blundy, and R. S. Sparks. The genesis of intermediate and silicic magmas in deep crustal hot zones. *Journal of Petrology*, 47(3):505–539, 2006. ISSN 00223530. doi: 10.1093/petrology/egi084.

W. Bach and G. L. Früh-Green. Alteration of the oceanic lithosphere and implications for seafloor processes. *Elements*, 6(3):173–178, 2010. ISSN 18115217. doi: 10.2113/gselements.6.3.173.

514 R. J. M. Baxter, J. Maclennan, D. A. Neave, and T. Thordarson. Depth of Magma Storage
515 Under Iceland Controlled by Magma Fluxes. *Geochemistry Geophysics Geosystems*, 2023.
516 doi: 10.1029/2022GC010811.

517 G. W. Boehlert. Current-topography interactions at mid-ocean seamounts and the impact
518 on pelagic ecosystems. *GeoJournal*, 16(1):45–52, 1988. ISSN 03432521. doi: 10.1007/
519 BF02626371.

520 J. W. Bown and R. S. White. Variation with spreading rate of oceanic crustal thickness and
521 geochemistry. *Earth*, 121:435–449, 1994. ISSN 10974547. doi: 10.1002/jnr.490190314.

522 M. Cannat, J. Cann, and J. Maclennan. Some hard rock constraints on the supply of heat
523 to mid-ocean ridges. *Geophysical Monograph Series*, 148:111–149, 2004. ISSN 23288779.
524 doi: 10.1029/148GM05.

525 S. Carbotte, C. Mutter, J. Mutter, and G. Ponce-Correa. Influence of magma supply and
526 spreading rate on crustal magma bodies and emplacement of the extrusive layer: insights
527 from the East Pacific Rise at lat 16°N. *Geology*, 26(5):455–458, 1998. ISSN 00917613. doi:
528 10.1130/0091-7613(1998)026<0455:IOMSAS>2.3.CO;2.

529 S. M. Carbotte, D. K. Smith, M. Cannat, and E. M. Klein. Tectonic and magmatic segmen-
530 tation of the Global Ocean Ridge System: A synthesis of observations. *Geological Society*
531 *Special Publication*, 420(1):249–295, 2016. ISSN 03058719. doi: 10.1144/SP420.5.

532 M. Cassidy, M. Manga, K. Cashman, and O. Bachmann. Controls on explosive-effusive
533 volcanic eruption styles. *Nature Communications*, 9(1), 2018. ISSN 20411723. doi: 10.
534 1038/s41467-018-05293-3.

535 J. Chen and J. P. Morgan. Rate , the Magma Budget , and the of Magma Emplacement.
536 *Journal of Geophysical Research*, 101:11475–11482, 1996.

Y. J. Chen. Influence of the Iceland mantle plume on crustal accretion at the inflated Reykjanes Ridge: Magma lens and low hydrothermal activity? *Journal of Geophysical Research*, 108(B11):1–12, 2003. ISSN 0148-0227. doi: 10.1029/2001jb000816.

G. L. Christeson, J. A. Goff, and R. S. Reece. Synthesis of Oceanic Crustal Structure From Two-Dimensional Seismic Profiles. *Reviews of Geophysics*, 57(2):504–529, 2019. ISSN 19449208. doi: 10.1029/2019RG000641.

C. A. Dalton, C. H. Langmuir, and A. Gale. Geophysical and Geochemical Evidence for Deep Temperature Variations Beneath Mid-Ocean Ridges. *Science*, 344(April):2–5, 2014.

F. A. Darbyshire, R. S. White, and K. F. Priestley. Structure of the crust and uppermost mantle of Iceland from a combined seismic and gravity study. *Earth and Planetary Science Letters*, 181(3):409–428, 2000. ISSN 0012821X. doi: 10.1016/S0012-821X(00)00206-5.

C. DeMets, R. G. Gordon, and D. F. Argus. Geologically current plate motions. *Geophysical Journal International*, 181(1):1–80, 2010. ISSN 0956540X. doi: 10.1111/j.1365-246X.2009.04491.x.

P. Einarsson. Plate boundaries , rifts and transforms in Iceland. *Jokull*, 58(58):35–58, 2008. ISSN 0449-0576.

H. Elderfield and A. Schultz. Mid-ocean ridge hydrothermal fluxes and the chemical composition of the ocean. *Annual Review of Earth & Planetary Sciences*, 24:191–224, 1996. ISSN 0084-6597. doi: 10.1146/annurev.earth.24.1.191.

A. Gale, C. A. Dalton, C. H. Langmuir, Y. Su, and J. G. Schilling. The mean composition of ocean ridge basalts. *Geochemistry, Geophysics, Geosystems*, 14(3):489–518, 2013. ISSN 15252027. doi: 10.1029/2012GC004334.

559 A. Gale, C. H. Langmuir, and C. A. Dalton. The global systematics of ocean ridge basalts
560 and their origin. *Journal of Petrology*, 55(6):1051–1082, 2014. ISSN 14602415. doi:
561 10.1093/petrology/egu017.

562 I. Garcia Berdeal, S. L. Hautala, L. N. Thomas, and H. Paul Johnson. Vertical structure
563 of time-dependent currents in a mid-ocean ridge axial valley. *Deep-Sea Research Part I:*
564 *Oceanographic Research Papers*, 53(2):367–386, 2006. ISSN 09670637. doi: 10.1016/j.dsr.
565 2005.10.004.

566 D. Giordano and D. B. Dingwell. Viscosity of hydrous Etna basalt: Implications for Plinian-
567 style basaltic eruptions. *Bulletin of Volcanology*, 65(1):8–14, 2003. ISSN 02588900. doi:
568 10.1007/s00445-002-0233-2.

569 M. L. M. Gleeson, S. A. Gibson, and M. J. Stock. Upper Mantle Mush Zones beneath Low
570 Melt Flux Ocean Island Volcanoes: Insights from Isla Floreana, Galápagos. *Journal of*
571 *Petrology*, 61(12):1–26, 2020. ISSN 14602415. doi: 10.1093/petrology/egaa094.

572 R. W. Griffiths. The dynamics of lava flows. *Annual Review of Fluid Mechanics*, 32:477–518,
573 2000. ISSN 00664189. doi: 10.1146/annurev.fluid.32.1.477.

574 T. L. Grove, R. J. Kinzler, and W. B. Bryan. Fractionation of Mid-Ocean Ridge Basalt
575 (MORB). *Geophysical Monograph*, 71:281–310, 1992. doi: 10.1029/gm071p0281.

576 M. E. Hartley, E. Bali, J. Maclennan, D. A. Neave, and S. A. Halldórsson. Melt
577 inclusion constraints on petrogenesis of the 2014–2015 Holuhraun eruption, Iceland.
578 *Contributions to Mineralogy and Petrology*, 173(2):1–23, 2018. ISSN 00107999. doi:
579 10.1007/s00410-017-1435-0. URL http://dx.doi.org/10.1007/s00410-017-1435-0.

580 J. Hasenclever, S. Theissen-Krah, L. H. Rüpke, J. P. Morgan, K. Iyer, S. Petersen, and C. W.
581 Devey. Hybrid shallow on-axis and deep off-axis hydrothermal circulation at fast-spreading
582 ridges. *Nature*, 508(7497):508–512, 2014. ISSN 14764687. doi: 10.1038/nature13174.

583 C. Herzberg. Partial crystallization of mid-ocean ridge basalts in the crust and mantle.
584 *Journal of Petrology*, 45(12):2389–2405, 2004. ISSN 00223530. doi: 10.1093/petrology/
585 egh040.

586 D. R. Hilton, M. F. Thirlwall, R. N. Taylor, B. J. Murton, and A. Nichols. Controls on
587 magmatic degassing along the Reykjanes Ridge with implications for the helium paradox.
588 *Earth and Planetary Science Letters*, 183(1-2):43–50, 2000. ISSN 0012821X. doi: 10.1016/
589 S0012-821X(00)00253-3.

590 Á. Höskuldsson, R. Hey, E. Kjartansson, and G. B. Gudmundsson. The Reykjanes Ridge
591 between 63°10N and Iceland. *Journal of Geodynamics*, 43(1):73–86, 2007. ISSN 02643707.
592 doi: 10.1016/j.jog.2006.09.003.

593 G. Ito, J. Lin, and D. Graham. Observational and theoretical studies of the dynamics of
594 mantle plume-mid-ocean ridge interaction. *Reviews of Geophysics*, 41(4), 2003. ISSN
595 87551209. doi: 10.1029/2002RG000117.

596 M. D. Jackson, J. Blundy, and R. S. J. Sparks. Chemical differentiation, cold storage and
597 remobilization of magma in the Earth's crust. *Nature*, 2018. ISSN 1476-4687. doi: 10.
598 1038/s41586-018-0746-2. URL http://dx.doi.org/10.1038/s41586-018-0746-2.

599 J. Jenkins, J. Maclennan, R. G. Green, S. Cottaar, A. F. Deuss, and R. S. White. Crustal
600 Formation on a Spreading Ridge Above a Mantle Plume: Receiver Function Imaging of the
601 Icelandic Crust. *Journal of Geophysical Research: Solid Earth*, 123(6):5190–5208, 2018.
602 ISSN 21699356. doi: 10.1029/2017JB015121.

603 S. M. Jones, N. White, and J. Maclennan. V-shaped ridges around Iceland: Implications for
604 spatial and temporal patterns of mantle convection. *Geochemistry, Geophysics, Geosys-*
605 *tems*, 3(10), 2002. ISSN 15252027. doi: 10.1029/2002GC000361.

S. M. Jones, B. J. Murton, J. G. Fitton, N. J. White, J. Maclennan, and R. L. Walters. A joint geochemical-geophysical record of time-dependent mantle convection south of Iceland. *Earth and Planetary Science Letters*, 386:86–97, 2014. ISSN 0012821X. doi: 10.1016/j.epsl.2013.09.029. URL http://dx.doi.org/10.1016/j.epsl.2013.09.029.

I. Kushiro. Melting of hydrous upper mantle and possible generation of andesitic magma: An approach from synthetic systems, 1974. ISSN 0012821X.

I. Kushiro, Y. Ikeda, and Y. Nakamura. Petrology of Apollo 14 hihg-alumina basalt. *Proceedings of the Third Lunar Science conference*, 1:115–129, 1972.

M. Le Saout, D. Pałgan, C. W. Devey, T. S. Lux, S. Petersen, D. Thorhallsson, A. Tomkowicz, and S. Brix. Variations in Volcanism and Tectonics Along the Hotspot-Influenced Reykjanes Ridge. *Geochemistry, Geophysics, Geosystems*, 24(4), 2023. ISSN 15252027. doi: 10.1029/2022GC010788.

C. E. Lesher and F. J. Spera. *Thermodynamic and Transport Properties of Silicate Melts and Magma*. Elsevier Inc., second edition edition, 2015. ISBN 9780123859389. doi: 10.1016/b978-0-12-385938-9.00005-5. URL http://dx.doi.org/10.1016/B978-0-12-385938-9.00005-5.

J. Lin and J. Phipps Morgan. The spreading rate dependence of three-dimensional mid-ocean ridge gravity structure. *Geophysical re*, 19(1):13–16, 1992.

R. P. Lowell, B. W. Crowell, K. C. Lewis, and L. Liu. Modeling Multiphase, Multicomponent Processes at Oceanic Spreading Centers. *Geophysical Monograph Series*, (178):15–44, 2008. ISSN 23288779. doi: 10.1029/178GM03.

K. Macdonald. Mid-ocean Ridge Tectonics, Volcanism And Geomorphology. *Encyclopedia of Ocean Sciences*, pages 1798–1813, 2001. doi: 10.1006/rwos.2001.0094.

J. Maclennan. The Supply of Heat to Mid-Ocean Ridges by Crystallization and Cooling of Mantle Melts. *Magma to Microbe: Modeling Hydrothermal Processes at Oceanic Spreading Centers*, pages 45–73, 2008. ISSN 23288779. doi: 10.1029/178GM04.

J. Maclennan, D. Mckenzie, and K. Gronvold. Plume-driven upwelling under Central Iceland. *Earth and Planetary Science Letters*, 194(1-2):67–82, 2001. ISSN 0012821X. doi: 10.1016/S0012-821X(01)00553-2.

M. Mazzocchi, F. Hansstein, and M. Ragona. The 2010 volcanic ash cloud and its financial impact on the European airline industry. *CESifo Forum*, 11(2):92–100, 2010. ISSN 1615245X.

P. J. Michael and R. L. Chase. The influence of primary magma composition, H2O and pressure on mid-ocean ridge basalt differentiation. *Contributions to Mineralogy and Petrology*, 96(2):245–263, 1987. ISSN 00107999. doi: 10.1007/BF00375237.

P. J. Michael and W. C. Cornell. Influence of spreading rate and magma supply on crystallization and assimilation beneath mid-ocean ridges: Evidence from chlorine and major element chemistry of mid-ocean ridge basalts. *Journal of Geophysical Research: Solid Earth*, 103(8):18325–18356, 1998. ISSN 21699356. doi: 10.1029/98jb00791.

J. B. Minster and T. H. Jordan. Present-day plate motion. *Journal of Geophysical Research*, 83, 1978.

J. P. Morgan and Y. J. Chen. Supply and Spreading Rate. *Letters to Nature*, 364(August): 706–708, 1993.

B. J. Murton, R. N. Taylor, and M. F. Thirlwall. Plume-Ridge Interaction: a Geochemical Perspective from the Reykjanes Ridge. *Journal of Petrology*, 43(11):1987–2012, 2002. ISSN 0022-3530. doi: 10.1093/petrology/43.11.1987.

C. A. Neal, S. R. Brantley, L. Antolik, J. L. Babb, and Etc. The 2018 rift eruption and summit collapse of Kīlauea Volcano. *Science*, 363(January):367–374, 2019.

D. A. Neave, J. Maclennan, T. Thordarson, and M. E. Hartley. The evolution and storage of primitive melts in the Eastern Volcanic Zone of Iceland: the 10 ka Grímsvötn tephra series (i.e. the Saksunarvatn ash). *Contributions to Mineralogy and Petrology*, 170(2):1–23, 2015. ISSN 00107999. doi: 10.1007/s00410-015-1170-3.

M. J. O'Hara. The bearing of phase equilibria studies in synthetic and natural systems on the origin and evolution of basic and ultrabasic rocks. *Earth Science Reviews*, 4(C): 69–133, 1968. ISSN 00128252. doi: 10.1016/0012-8252(68)90147-5. URL http://dx.doi.org/10.1016/0012-8252(68)90147-5.

D. Pałgan, C. W. Devey, and I. A. Yeo. Volcanism and hydrothermalism on a hotspot–influenced ridge: Comparing Reykjanes Peninsula and Reykjanes Ridge, Iceland. *Journal of Volcanology and Geothermal Research*, 348:62–81, 2017. ISSN 03770273. doi: 10.1016/j.jvolgeores.2017.10.017.

K. S. Panter, P. Castillo, S. Krans, C. Deering, W. McIntosh, J. W. Valley, K. Kitajima, P. Kyle, S. Hart, and J. Blusztajn. Melt Origin across a Rifted Continental Margin: a Case for Subduction-related Metasomatic Agents in the Lithospheric Source of Alkaline Basalt, NW Ross Sea, Antarctica. *Journal of Petrology*, 59(3):517–558, 2018. ISSN 0022-3530. doi: 10.1093/petrology/egy036. URL https://academic.oup.com/petrology/article/59/3/517/4966906.

R. Parnell-Turner, N. White, T. Henstock, B. Murton, J. Maclennan, and S. M. Jones. A continuous 55-million-year record of transient mantle plume activity beneath Iceland. *Nature Geoscience*, 7(12):914–919, 2014. ISSN 17520908. doi: 10.1038/ngeo2281.

675 R. Parnell-Turner, N. White, T. J. Henstock, S. M. Jones, J. Maclennan, and B. J. Murton.
676 Causes and Consequences of Diachronous V-Shaped Ridges in the North Atlantic Ocean.
677 *Journal of Geophysical Research: Solid Earth*, 122(11):8675–8708, 2017. ISSN 21699356.
678 doi: 10.1002/2017JB014225.

679 R. E. Parnell-Turner, N. J. White, J. MacLennan, T. J. Henstock, B. J. Murton, and S. M.
680 Jones. Crustal manifestations of a hot transient pulse at 60°N beneath the Mid-Atlantic
681 Ridge. *Earth and Planetary Science Letters*, 363:109–120, 2013. ISSN 0012821X. doi:
682 10.1016/j.epsl.2012.12.030. URL http://dx.doi.org/10.1016/j.epsl.2012.12.030.

683 L. Parson, B. Murton, R. Searle, D. Booth, J. Evans, P. Field, J. Keeton, A. Laughton,
684 E. McAllister, N. Millard, L. Redbourne, I. Rouse, A. Shor, D. Smith, S. Spencer, C. Sum-
685 merhayes, and C. Walker. En echelon axial volcanic ridges at the Reykjanes Ridge: a life
686 cycle of volcanism and tectonics. *Earth and Planetary Science Letters*, 117:73–87, 1993.

687 S. R. Paterson, D. Okaya, V. Memeti, R. Economos, and R. B. Miller. Magma addition
688 and flux calculations of incrementally constructed magma chambers in continental margin
689 arcs: Combined field, geochronologic, and thermal modeling studies. *Geosphere*, 7(6):
690 1439–1468, 2011. ISSN 1553-040. doi: 10.1130/GES00696.1.

691 J. Phipps Morgan and Y. J. Chen. Magma Injection , Hydrothermal Circulation , and
692 Crustal Flow. *Journal of Geophysical Research*, 98(B4):6283–6297, 1993.

693 R. Poreda, J. G. Schilling, and H. Craig. Helium and hydrogen isotopes in ocean-ridge basalts
694 north and south of Iceland. *Earth and Planetary Science Letters*, 78(1):1–17, 1986. ISSN
695 0012821X. doi: 10.1016/0012-821X(86)90168-8.

696 G. Purdy, L. Kong, G. L. Christeson, and S. Solomon. Relationship between spreading rate
697 and the seismic structure of mid-ocean ridges. *Letters to Nature*, 355(5505):815–817, 1992.
698 ISSN 00280836. doi: 10.1038/255242a0.

699 D. T. Sandwell and W. H. Smith. Global marine gravity from retracked Geosat and ERS-1
700 altimetry: Ridge segmentation versus spreading rate. *Journal of Geophysical Research:*
701 *Solid Earth*, 114(1):1–18, 2009. ISSN 21699356. doi: 10.1029/2008JB006008.

702 J.-G. Schilling. Iceland mantle plume: geochemical evidence along Reykjanes Ridge. *Nature*,
703 242(5400):565–571, 1973. URL https://www.nature.com/articles/242565a0.

704 J. M. Scott, T. E. Waight, Q. H. Van Der Meer, J. M. Palin, A. F. Cooper, and C. Münker.
705 Metasomatized ancient lithospheric mantle beneath the young Zealandia microcontinent
706 and its role in HIMU-like intraplate magmatism. *Geochemistry, Geophysics, Geosystems*,
707 15(9):3474–3501, 2014. ISSN 15252027. doi: 10.1002/2014GC005300.

708 J. M. Scott, A. Pontesilli, M. Brenna, J. D. White, E. Giacalone, J. M. Palin, and P. J.
709 le Roux. The Dunedin Volcanic Group and a revised model for Zealandia's alkaline in-
710 traplate volcanism, 2020. ISSN 11758791. URL https://doi.org/10.1080/00288306.2019.
711 1707695.

712 R. C. Searle, J. Keeton, R. B. Owens, R. S. White, R. Mecklenburgh, P. Parsons, and
713 S. Lee. The Reykjanes Ridge: structure and tectonics of a hot-spot influenced, slow-
714 spreading ridge, from multibeam bathymetry, gravity and magnetic investigation. *Earth*
715 *and Planetary Science Letters*, 1998:2446–2448, 1998. doi: 10.1109/PAC.2005.1591140.

716 R. C. Searle, B. J. Murton, K. Achenbach, T. LeBas, M. Tivey, I. Yeo, M. H. Cormier,
717 J. Carlut, P. Ferreira, C. Mallows, K. Morris, N. Schroth, P. van Calsteren, and C. Waters.
718 Structure and development of an axial volcanic ridge: Mid-Atlantic Ridge, 45°N. *Earth*
719 *and Planetary Science Letters*, 299(1-2):228–241, 2010. ISSN 0012821X. doi: 10.1016/j.
720 epsl.2010.09.003. URL http://dx.doi.org/10.1016/j.epsl.2010.09.003.

721 O. Shorttle, J. MacLennan, and S. M. Jones. Control of the symmetry of plume-ridge

722 interaction by spreading ridge geometry. *Geochemistry, Geophysics, Geosystems*, 11(7):
723 1–27, 2010. ISSN 15252027. doi: 10.1029/2009GC002986.

724 N. H. Sleep. Formation of Oceanic Crust: Some Thermal Constrains. 80(29):4037–4042,
725 1975.

726 J. R. Smallwood and R. S. White. Crustal accretion at the Reykjanes thickness is 400 + 100
727 m The velocity at the base. 103:5185–5201, 1998.

728 H. Soosalu, K. Jónsdóttir, and P. Einarsson. Seismicity crisis at the Katla volcano, Iceland-
729 signs of a cryptodome? *Journal of Volcanology and Geothermal Research*, 153(3-4):177–
730 186, 2006. ISSN 03770273. doi: 10.1016/j.jvolgeores.2005.10.013.

731 H. Soosalu, J. Key, R. S. White, C. Knox, P. Einarsson, and S. S. Jakobsdóttir. Lower-
732 crustal earthquakes caused by magma movement beneath Askja volcano on the north
733 Iceland rift. *Bulletin of Volcanology*, 72(1):55–62, 2010. ISSN 02588900. doi: 10.1007/
734 s00445-009-0297-3.

735 S. A. Soule. *Mid-Ocean Ridge Volcanism*. Elsevier Inc., second edi edition, 2015. ISBN
736 9780123859389. doi: 10.1016/b978-0-12-385938-9.00021-3. URL http://dx.doi.org/10.
737 1016/B978-0-12-385938-9.00021-3.

738 M. Talwani, C. C. Windisch, and M. G. Langseth. Reykjanes idge crest. A detailed geophys-
739 ical study. *Journal of Geophysical Research*, 76(2):473–517, 1971. ISSN 2156-2202. doi:
740 10.1029/jb076i002p00473.

741 T. Thordarson and G. Larsen. Volcanism in Iceland in historical time: Volcano types,
742 eruption styles and eruptive history. *Journal of Geodynamics*, 43(1):118–152, 2007. ISSN
743 02643707. doi: 10.1016/j.jog.2006.09.005.

D. Tian, L. Uieda, W. J. Leong, W. Schlitzer, Y. Fröhlich, M. Grund, M. Jones, L. Toney, J. Yao, Y. Magen, J.-H. Tong, K. Materna, A. Belem, T. Newton, A. Anant, M. Ziebarth, J. Quinn, and P. Wessel. PyGMT: A Python interface for the Generic Mapping Tools, Sept. 2023. URL https://doi.org/10.5281/zenodo.8303186.

P. R. Vogt. Asthenosphere motion recorded by the ocean floor south of Iceland. *Earth and Planetary Science Letters*, 13(1):153–160, 1971. ISSN 0012821X. doi: 10.1016/0012-821X(71)90118-X.

M. Voigt, L. A. Coogan, and A. von der Handt. Experimental investigation of the stability of clinopyroxene in mid-ocean ridge basalts: The role of Cr and Ca/Al. *Lithos*, 274-275: 240–253, 2017. ISSN 18726143. doi: 10.1016/j.lithos.2017.01.003. URL http://dx.doi.org/10.1016/j.lithos.2017.01.003.

V. D. Wanless and M. D. Behn. Spreading rate-dependent variations in crystallization along the global mid-ocean ridge system. *Geochemistry, Geophysics, Geosystems*, 18(8):3016–3033, 2017. ISSN 15252027. doi: 10.1002/2017GC006924.

N. R. W. Weir, R. S. White, B. Brandsdóttir, P. Einarsson, H. Shimamura, and H. Shiobara. Crustal structure of the northern Reykjanes Ridge and Reykjanes Peninsula, southwest Iceland. *Journal of Geophysical Research: Solid Earth*, 106(B4):6347–6368, 2001. ISSN 2169-9356. doi: 10.1029/2000jb900358.

O. M. Weller, A. Copley, W. G. R. Miller, R. M. Palin, and B. Dyck. The relationship between mantle potential temperature and oceanic lithosphere buoyancy. *Earth and Planetary Science Letters*, 518:86–99, 2019. ISSN 0012-821X. doi: 10.1016/j.epsl.2019.05.005. URL https://doi.org/10.1016/j.epsl.2019.05.005.

R. S. White and D. McKenzie. Mantle plumes and flood basalts. *Journal of Geophysical Research*, 100(B9), 1995. ISSN 01480227. doi: 10.1029/95jb01585.

R. B. Whitmarsh and A. J. Calvert. Crustal structure of Atlantic fracture zones – I. The Charlie-Gibbs Fracture Zone. *Geophysical Journal of the Royal Astronomical Society*, 85 (1):107–138, 1986. ISSN 1365246X. doi: 10.1111/j.1365-246X.1986.tb05174.x.

H.-j. Yang, R. J. Kinzler, and T. L. Grove. Experiments and models of anhydrous, basaltic olivine-plagioclase-augite saturated melts from 0.001 to 10 kbar. *Contributions to Mineralogy and Petrology*, (124):1–18, 1996.

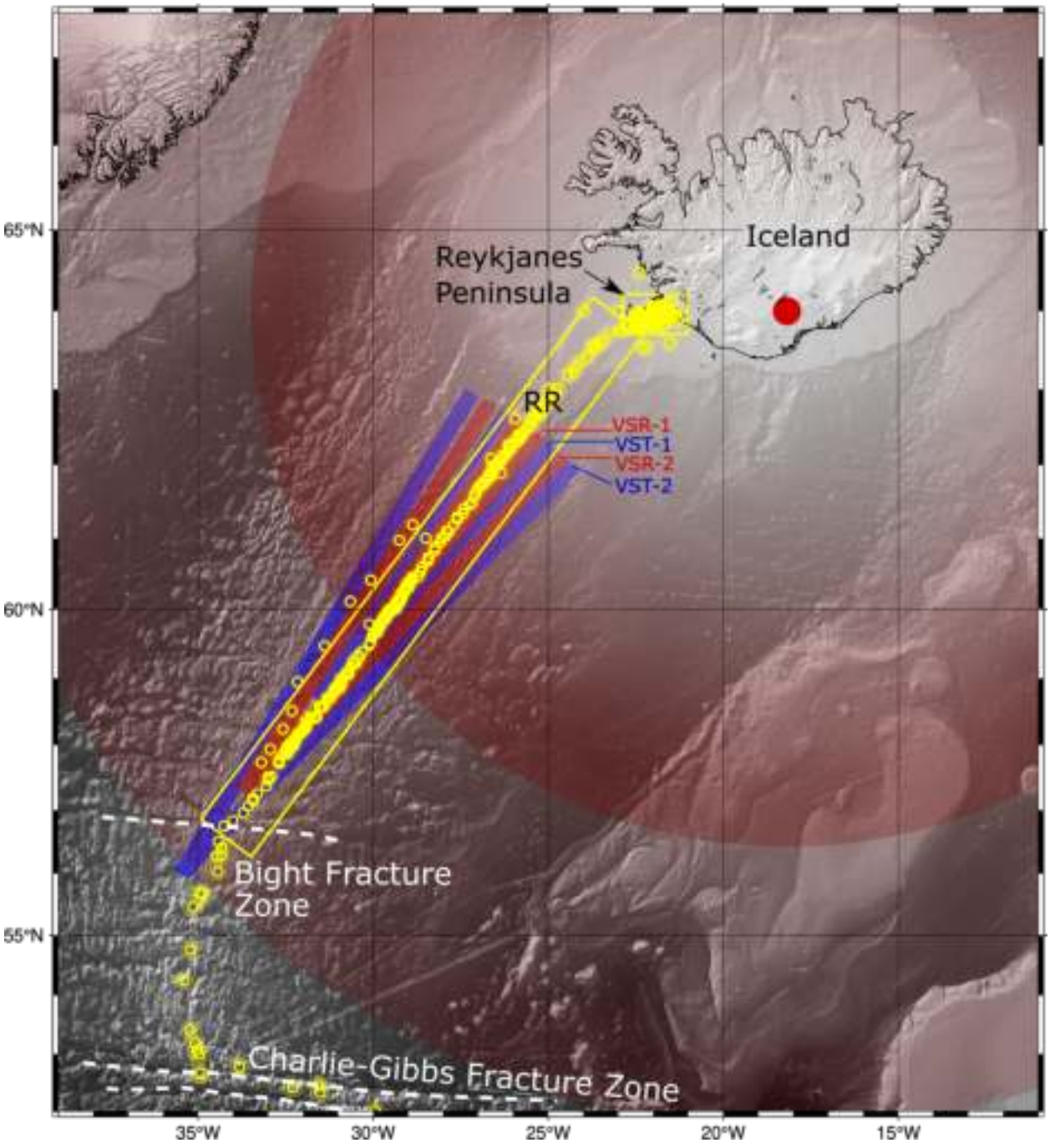

Figure 1: Bathymetric map of North Atlantic mid-ocean ridge segment focused on in this study, including the Reykjanes Peninsula of Iceland, the Reykjanes Ridge (RR), the Bight Fracture Zone, and the Charlie-Gibbs Fracture Zone. Red lines indicate the approximate locations of the V-shaped ridges (VSR-1 and VSR-2), while blue lines indicate V-shaped-troughs (VST-1 and VST-2). Yellow circles are the localities of all 1582 samples used in this study before filtering. The red dot indicates the approximate position of the Icelandic plume from (Shorttle et al., 2010). Large red circles/shading indicate the extent of the thermal and chemical influence of the mantle plume, and darker red shading indicates where the youngest V-shaped ridge intersects the RR, according to (Parnell-Turner et al., 2013; Jones et al., 2014)

.

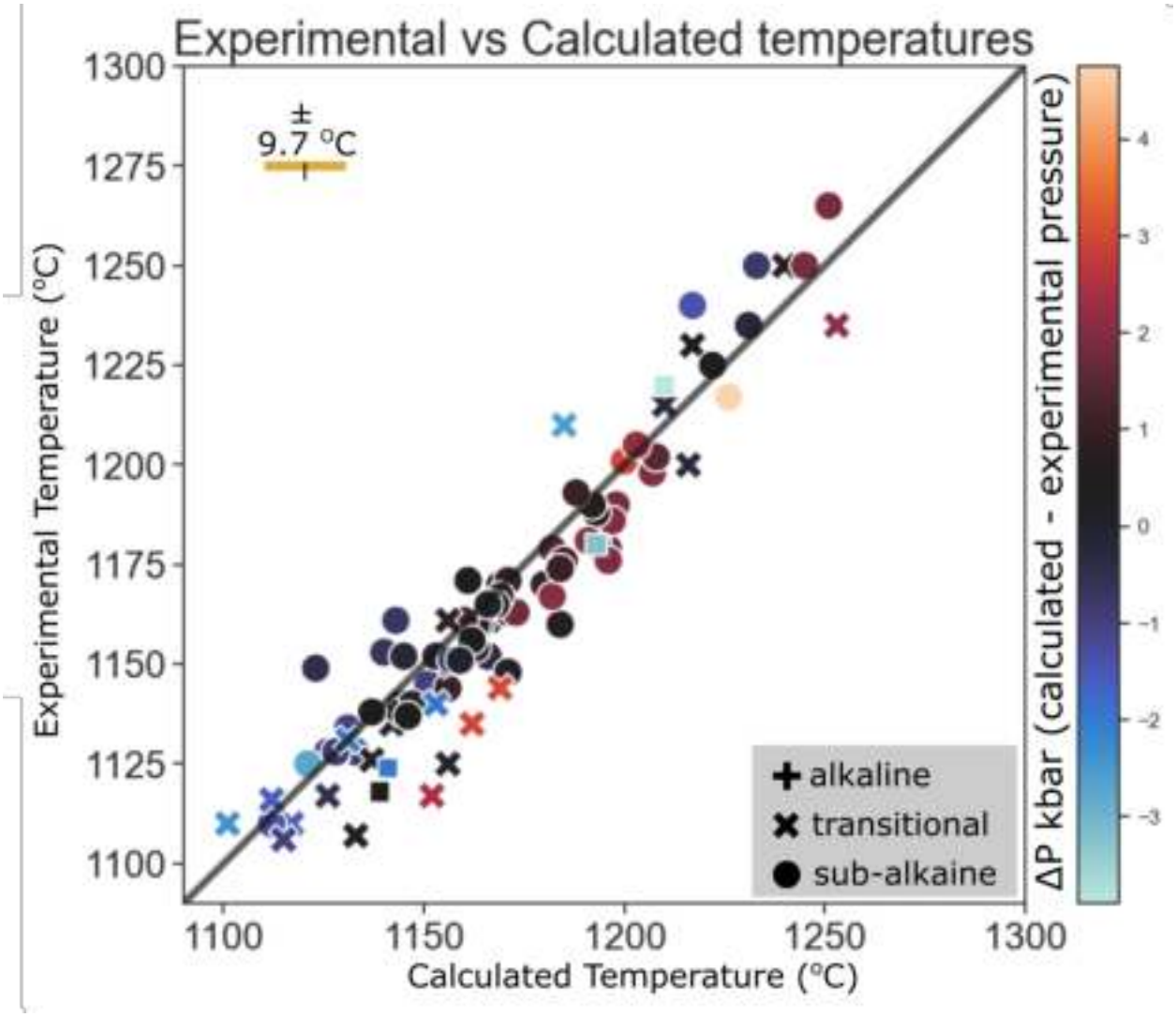

Figure 2: The addition of the probability filter improves the reliability and constrains the error of the OPAM thermobarometer compared to earlier iterations (Grove et al., 1992; Yang et al., 1996). (Baxter et al., 2023) constrained the pressure 1 σ to 1.16 kbar, and here we constrain the temperature 1 σ 9.7°C. Symbol colour is the ΔP, the difference between calculated and experimental pressure of samples.

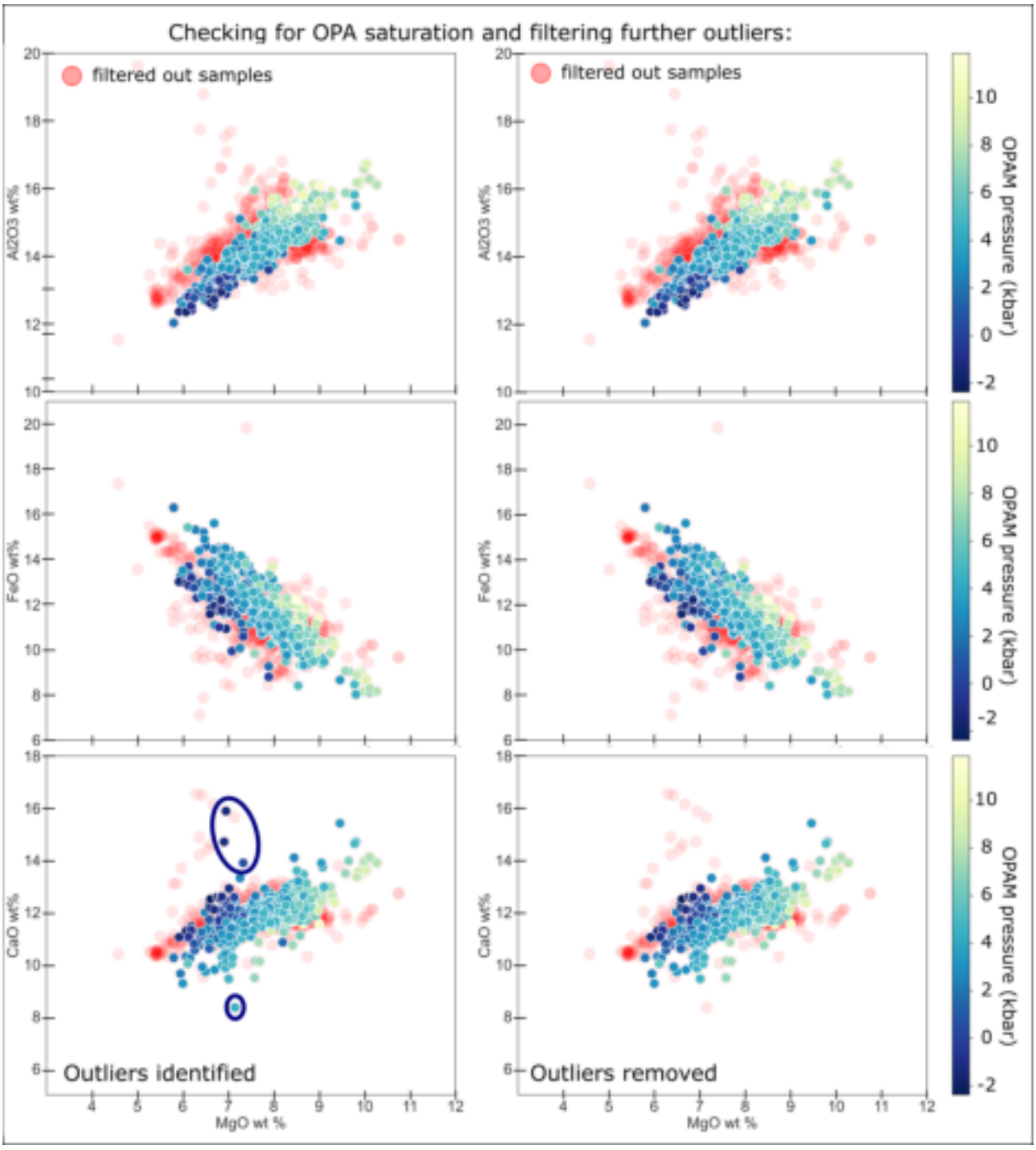

Figure 3: Distributions of CaO, FeO, and Al_2O_3 wt% against MgO wt% to identify samples that deviate from olivine–plagioclase–clinopyroxene saturation that may have slipped past compositional and probability filters in the pyOPAM script. Samples which deviate away from a fractionation trend controlled by olivine–plagioclase–augite saturation and fractionation are removed. Left-hand side shows samples after probability filter, where some outliers are probably due to crystal accumulation in whole-rock analyses. Right-hand side shows samples after outliers are identified and removed. The colour bar gives pressure estimates for samples in kbar (1 σ 1.16 kbar).

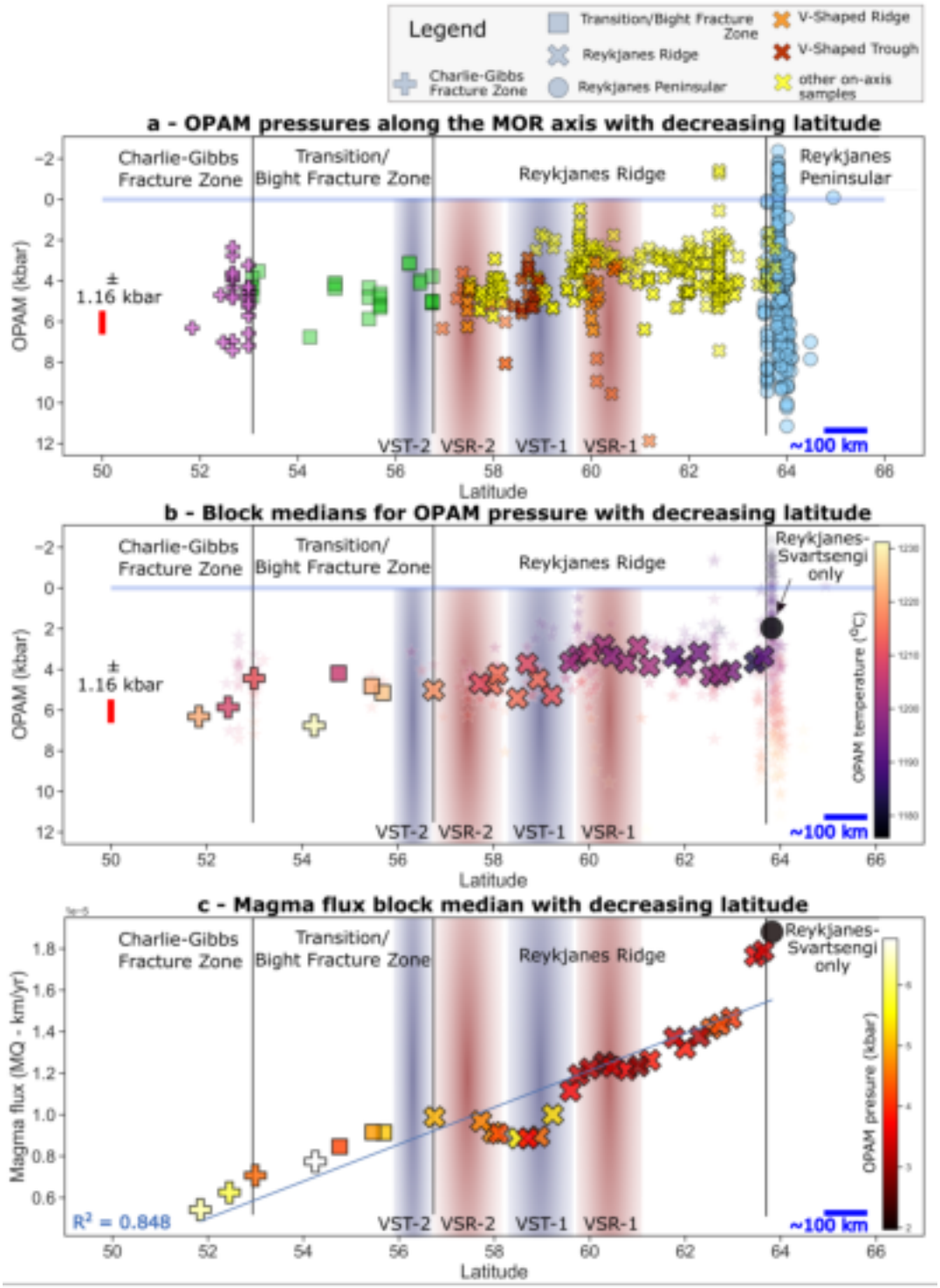

Figure 4: a) Storage pressure estimates for on-axis samples after pyOPAM filtering. Red and blue vertical lines mark the V-shaped ridges (VSRs) and V-shaped troughs (VSTs), respectively. Reykjanes Peninsula displays the widest range of pressure estimates. b) Median final depth of storage from 50 km × 15 km segments along the RR, and immediately adjacent segments (Reykjanes Peninsula, Transition/Bight Fracture Zone, and Charlie-Gibbs Fracture Zone). pyOPAM temperature estimates increase with increasing pressure. The median final depth and temperature of magma storage increase southwards away from Iceland. c) Magma flux estimates from the end of the Reykjanes Peninsula to the Charlie-Gibbs Fracture Zone. After the Reykjanes Peninsula, magma flux steadily decreases southwards, slightly increasing and decreasing where the RR is intersected by VSRs and VSTs.

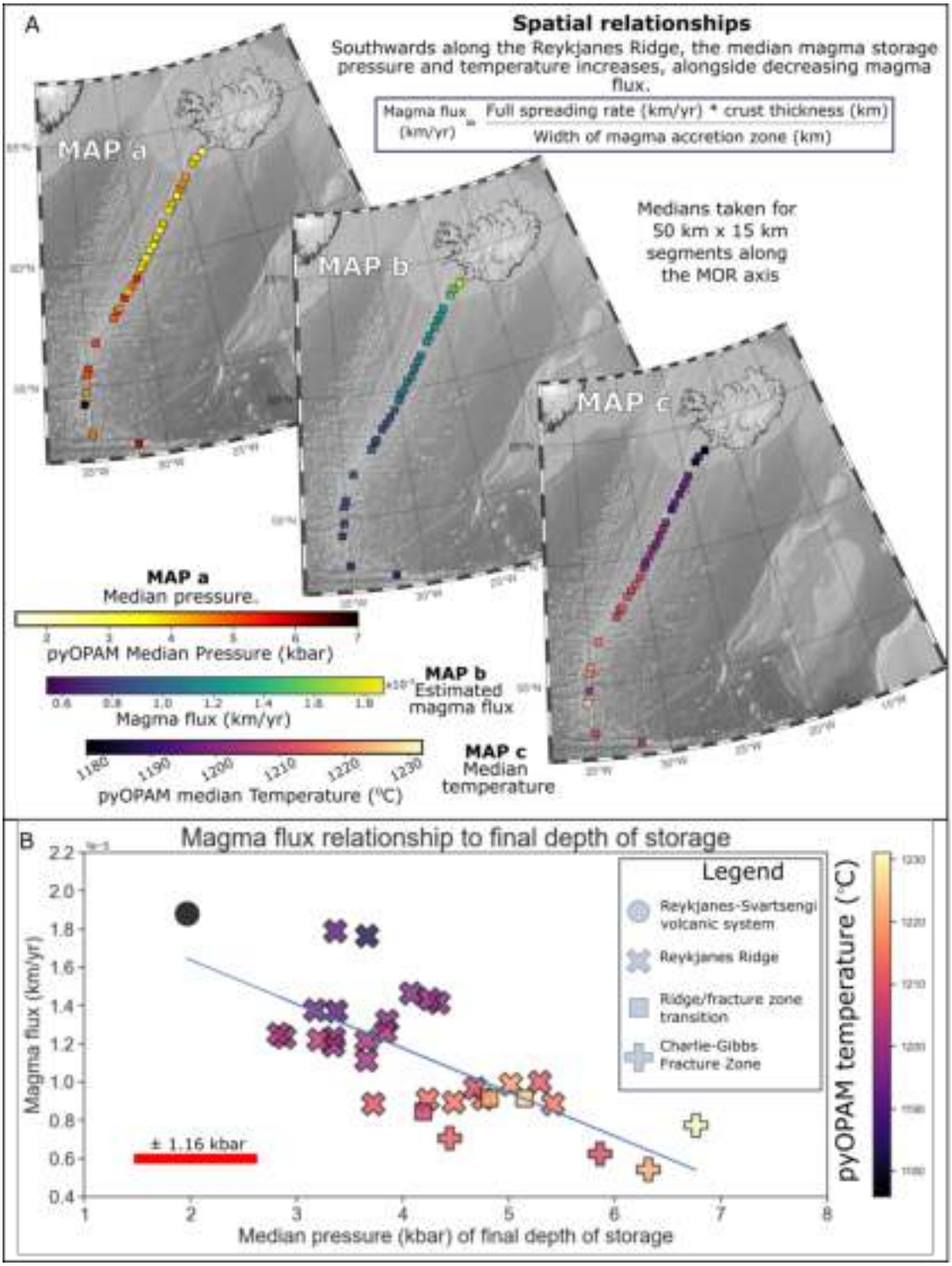

Figure 5: a) Spatial variability maps for median final depths of storage (Map a), estimated magma flux (Map b), and median temperatures (Map c) along the Reykjanes Ridge. Southwards along the Reykjanes Ridge, the median magma storage pressure and temperature increase alongside decreasing magma flux. Increasing magma storage pressures coincide with fluctuating magma flux, rather than with steady spreading rates (Minster and Jordan, 1978; DeMets et al., 2010) along the MOR, which has previously been stated to be the control on magma storage depths at MORs (Christeson et al., 2019; Wanless and Behn, 2017; Carbotte et al., 2016; Phipps Morgan and Chen, 1993; Morgan and Chen, 1993). b) Median pyOPAM pressures for 50 km segments, plotted against the estimated annual magma flux of the MOR segments, display a linear relationship.

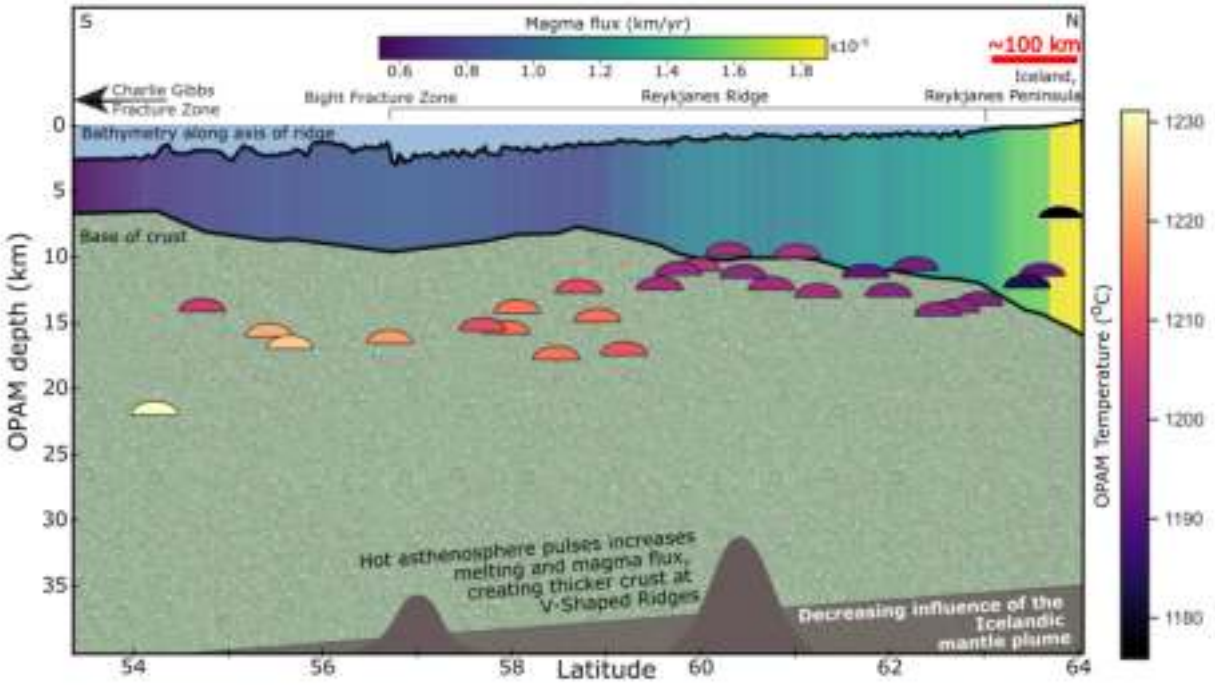

Figure 6: Summary figure for distributions of final magma storage depths and temperatures along the Reykjanes Ridge and adjacent segments of the North Atlantic Ridge. Crust colour indicates the estimated magma flux for 50 km long segments. Crustal thickness and magma flux decreases away from Iceland (Jones et al., 2014; Weir et al., 2001). Half-spreading rate remains at 10 mm/y $\pm$ 1 mm (Minster and Jordan, 1978; DeMets et al., 2010), yet crust thickness fluctuates. V-shaped ridges correspond with thicker crust where pulses of hot asthenosphere increase melt production. Pressure to depth conversion is based on a density of 3000 km/m^3 for oceanic crust, or if the depth exceeds 8 km (average thickness of oceanic crust), 3300 km/m^3 for mantle density is then used for depths exceeding. Values used from (Weller et al., 2019). Further calculation details can be found in text and the supplementary code.

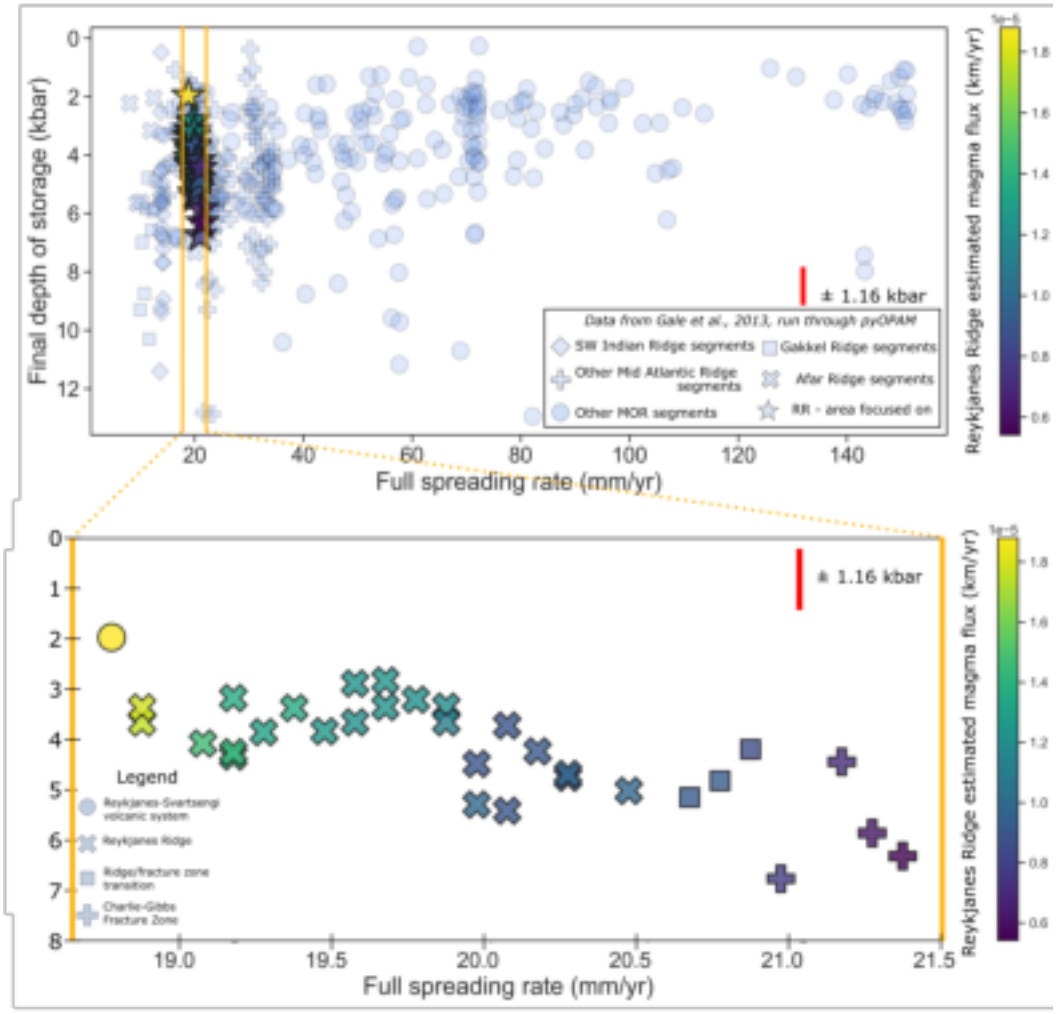

Figure 7: OPAM pressure estimates vs. spreading rate at MOR segments (global dataset from Gale et al. (2013)). Slow-spreading ridges highlighted as comparisons with the Reykjanes Ridge, including the Gakkel Ridge, SW Indian Ridge, other segments of the Mid-Atlantic Ridge, and Afar. With increasing spreading rate, the range of storage pressures decreases, becoming mostly shallow at faster-spreading rates. Shallow and deep storage pressures are observed for slow-spreading ridges. Counter to what has been established in the MOR literature, along the Reykjanes Ridge, magma storage pressures increase with the increasing spreading rate. On this ridge, storage depths decrease with increasing magma flux rather than increasing spreading rates.